

## Supplemental Information for

### Smelting-Rolling Strategy for ZnIn Bulk Phase Alloy Anode

Yizhao Chai <sup>a</sup>, Xuesong Xie <sup>a</sup>, Zhangxing He<sup>\*,b</sup>, Guangyi Guo <sup>c</sup>, Pinji Wang <sup>a</sup>, Zhenyue Xing <sup>a</sup>,

Bingan Lu <sup>d</sup>, Shuquan Liang <sup>a</sup>, Yan Tang<sup>\*,a</sup>, and Jiang Zhou<sup>\*,a,e</sup>

<sup>a</sup> School of Materials Science and Engineering, Hunan Provincial Key Laboratory of Electronic Packaging and Advanced Functional Materials, Central South University, Changsha 410083, China. E-mail: ty\_csu@csu.edu.cn; zhou\_jiang@csu.edu.cn

<sup>b</sup> School of Chemical Engineering, North China University of Science and Technology, Tangshan 063009, China. Email: zxhe@ncst.edu.cn

<sup>c</sup> School of Materials Science and Engineering, Hunan Provincial Key Laboratory of Nonferrous Materials Science and Engineering, Central South University, Changsha 410083, China.

<sup>d</sup> School of Physics and Electronics, Hunan University, Changsha 410082, China.

<sup>e</sup> College of Chemistry and Chemical Engineering, Jishou University, Jishou 416000, China.

## Supplementary Figures and captions

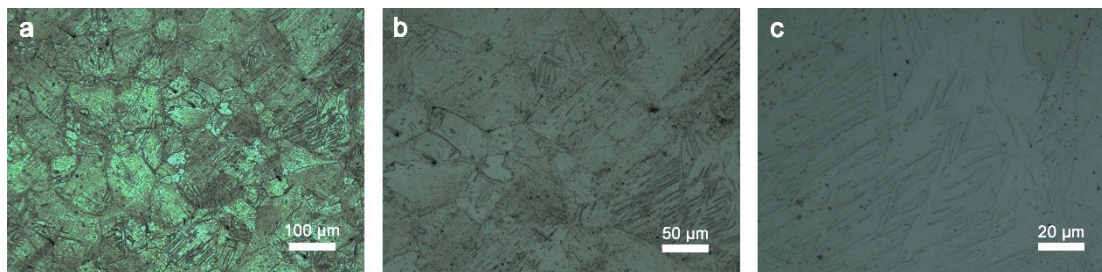


**Fig. S1** The optical microscope images of ZnIn alloy with different scales.

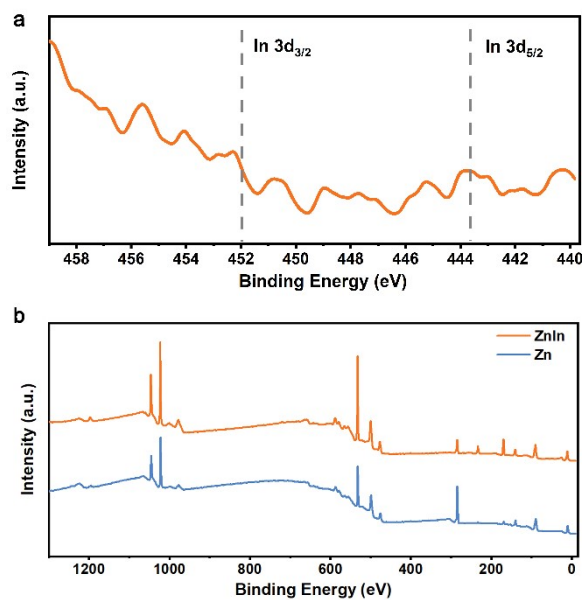


**Fig. S2** (a) High-resolution XPS spectra of In 3d for ZnIn alloy. (b) Full XPS peaks for ZnIn alloy and pure Zn.

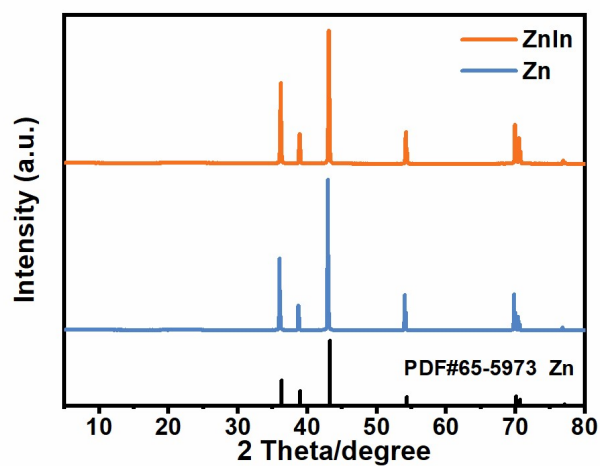


Fig. S3 XRD patterns of ZnIn alloy and pure Zn.

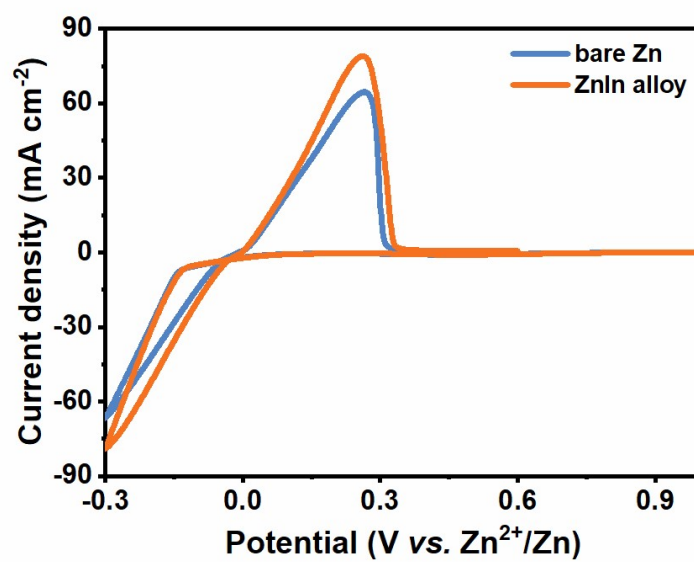
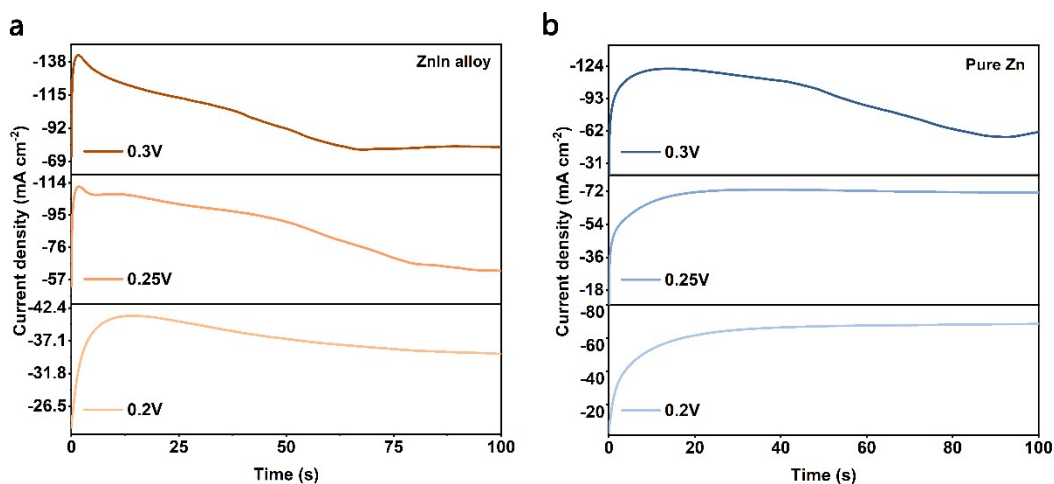
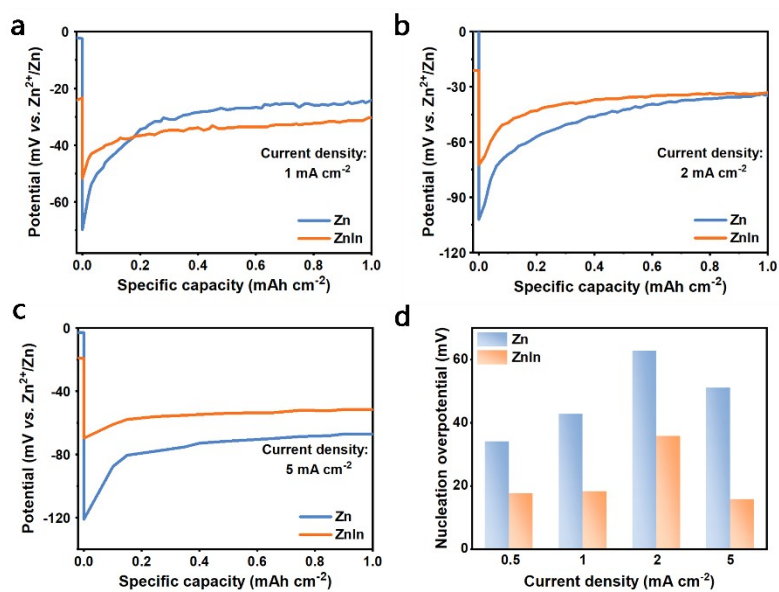


Fig. S4 Cyclic voltammetry (CV) curves of pure Zn//SS and ZnIn alloy//SS batteries at  $1 \text{ mV s}^{-1}$ .



**Fig. S5** Chronoamperograms measured at a series of potentials for (a) ZnIn alloy and (b) pure Zn.



**Fig. S6** Galvanostatic nucleation overpotential for ZnIn alloy and pure Zn at different density of (a) 1.0 mA cm<sup>-2</sup>, (b) 2.0 mA cm<sup>-2</sup>, (c) 5.0 mA cm<sup>-2</sup>. (d) Histogram comparison of the corresponding nucleation overpotential.

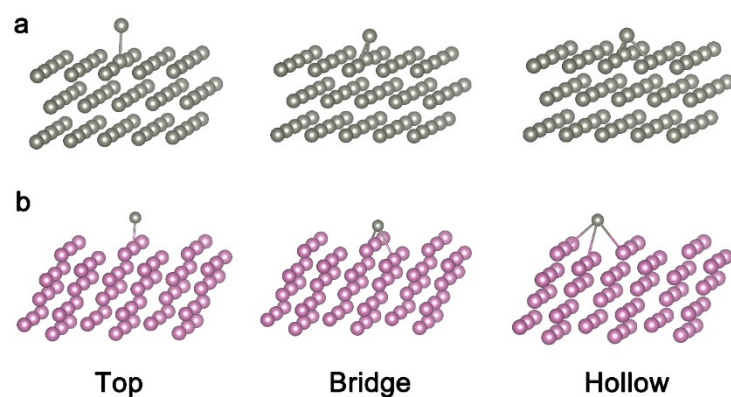


**Fig. S7** The adsorption of Zn and indium substrates to Zn atom at different adsorption sites. The Grey ball represents Zn atom and the pink ball represents indium atom.

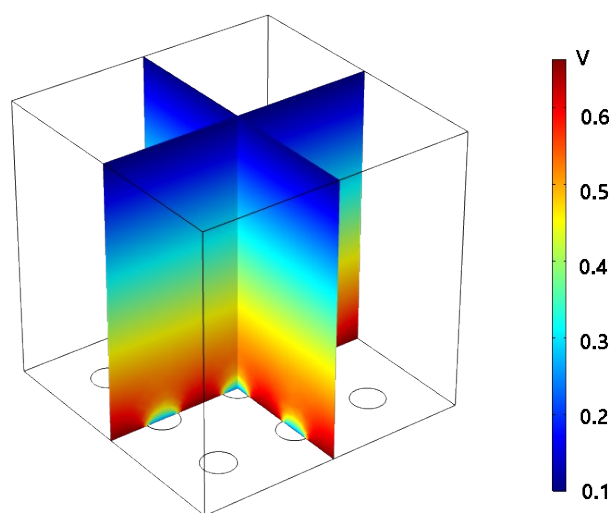


**Fig. S8** The electrolyte potential distribution during Zn deposition on ZnIn alloy by finite element method. The circles at the bottom represent indium element.

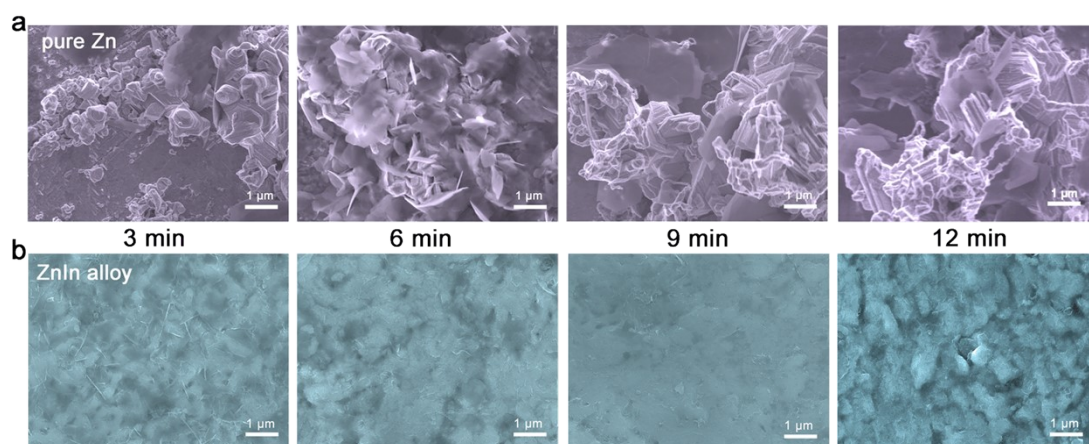


**Fig. S9** The morphology of Zn depositing on (a) pure Zn and (b) ZnIn alloy for 3, 6, 9 and 12 min at the current density of  $1 \text{ mA cm}^{-2}$ .

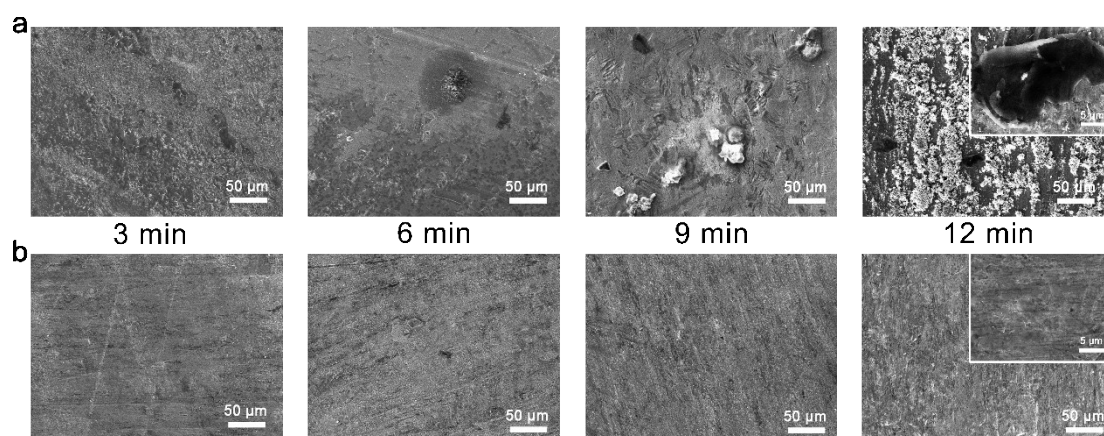


**Fig. S10** The morphologies of Zn stripping from (a) pure Zn and (b) ZnIn alloy for 3, 6, 9 and 12 min at the current density of  $1 \text{ mA cm}^{-2}$ .

In Fig. S10, The ZnIn alloy anode has a relatively flat surface and no obvious preferential stripping site. Reciprocally, with the increasing of stripping time, the voids and the dendrites on voids gradually appear, explaining the uneven dissolution of the pure Zn. The dendrites on the voids will gradually increase in size without disappearing during subsequent deposition and cycling. This may be because of the selection deposition of Zn while deposition. According to the Nernst equation, the concentration of  $\text{Zn}^{2+}$  in the micro-void is relatively sparse<sup>1</sup>, resulting in little deposition in the micro-void, when stripping, Zn will prefer stripping off from the micro-void, causing the micro-void to gradually grow larger. When the battery uses pure Zn anode cycles for a long time, there will appear many large voids on the surface of Zn anode.

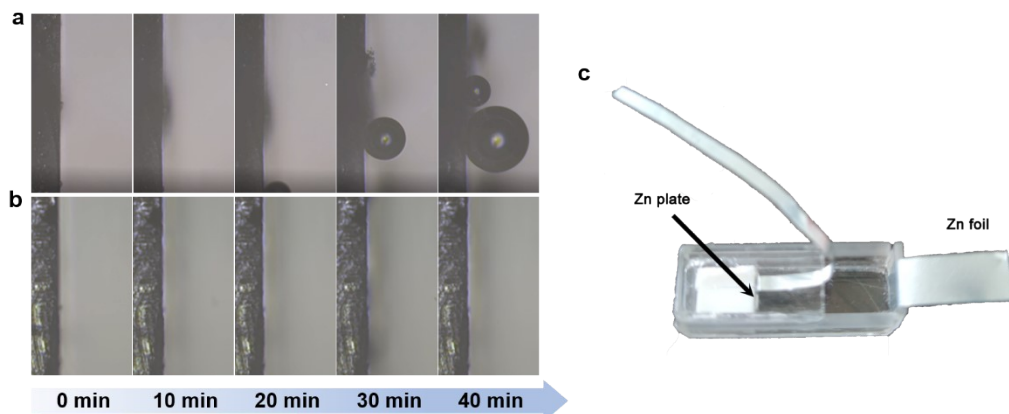


**Fig. S11** *In situ* OM visualization of Zn plating on (a) pure Zn and (b) ZnIn alloy at a high current of 10 mA. (c) Optical photograph of the *in situ* OM device.

To ensure that the current density of deposition for pure Zn and ZnIn alloy are the same, we use a device shown in Fig. S11 c. The area of the Zn plate is 0.24 cm<sup>2</sup>.

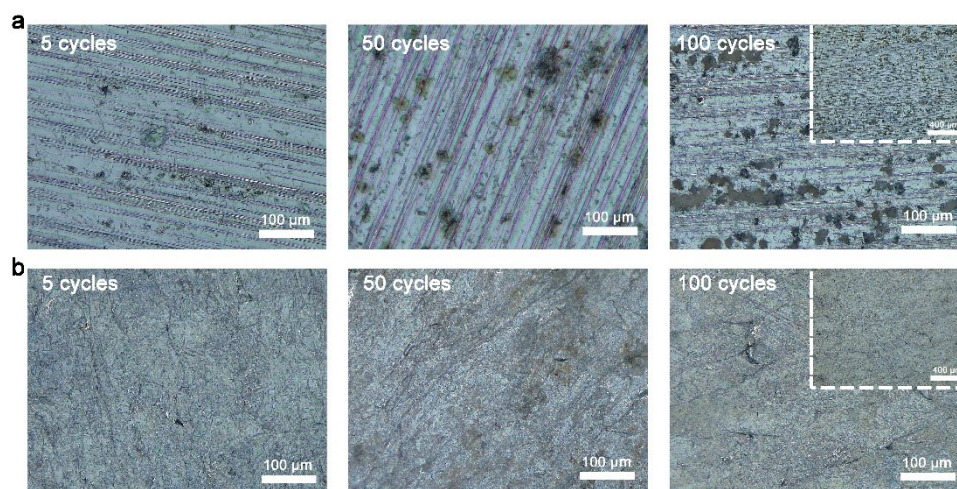


**Fig. S12** The morphology of (a) pure Zn and (b) ZnIn alloy after 5, 50 and 100 cycles respectively on OM.

As shown in Fig. S12, a well-preserved and integrated morphology is realized by the ZnIn alloy, while more and more voids are discovered with the increase of the number of cycles in pure Zn and are getting larger and larger.

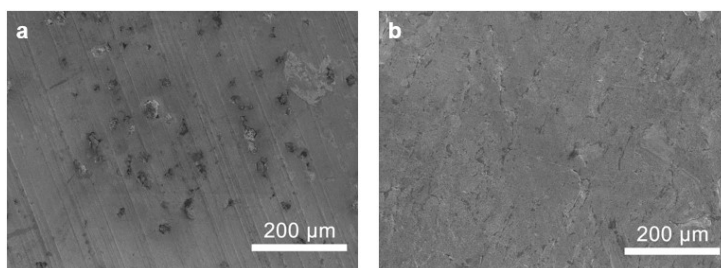


**Fig. S13** SEM images of (a) pure Zn and (b) ZnIn alloy after 100 cycles.

As shown in Fig. S13, the pure Zn after 100 cycles arises the cliffy dendrite pieces and by-product aggregations on the voids, this may be due to the tip effect. compare to the bottom of the dendrite, the current density and concentration at the top of Zn dendrite are larger, resulting in more deposition of Zn, and leads to less deposition around the bottom of Zn dendrite, resulting in larger voids. When the size of dendrites exceeds the critical point, they will fall off and become dead Zn, decreasing the CE and the utilization of Zn anode.

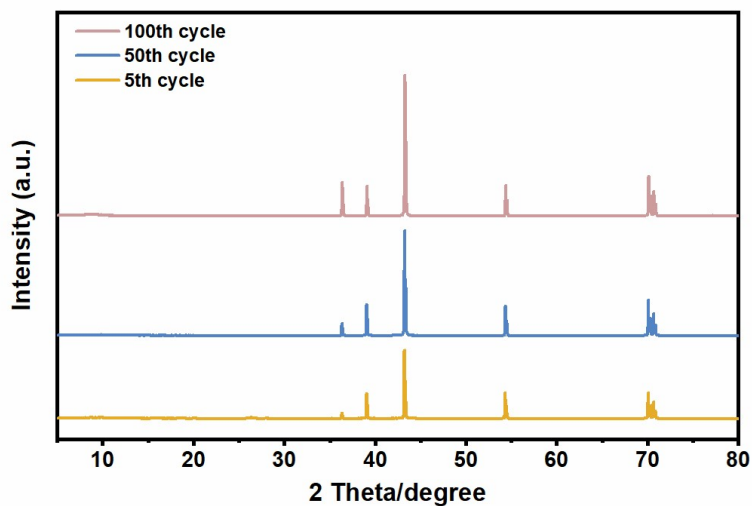


**Fig. S14** XRD patterns of ZnIn alloy after 5<sup>th</sup>, 50<sup>th</sup> and 100<sup>th</sup> cycles.

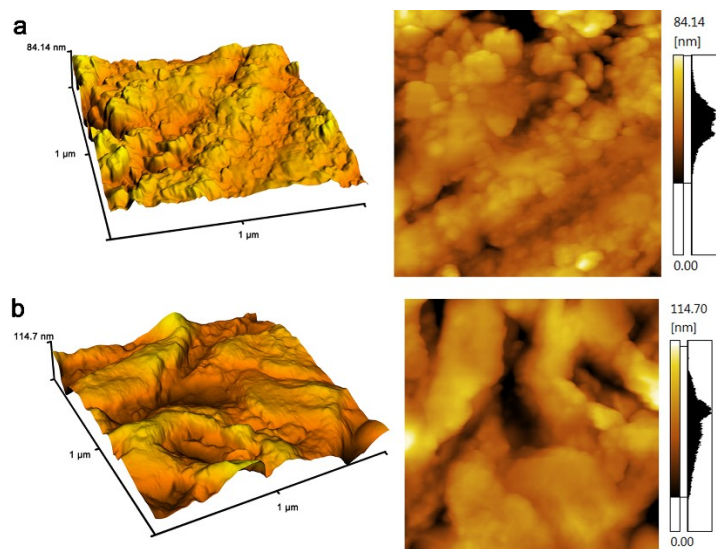


**Fig. S15** The morphologies of (a) ZnIn alloy anode and (b) pure Zn anode after 100 cycles.

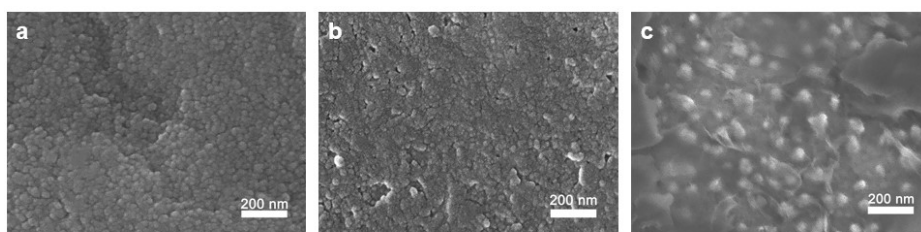


**Fig. S16** The nucleation morphologies of ZnIn alloy after (a) 5 cycles, (b) 50 cycles and (c) 100 cycles.

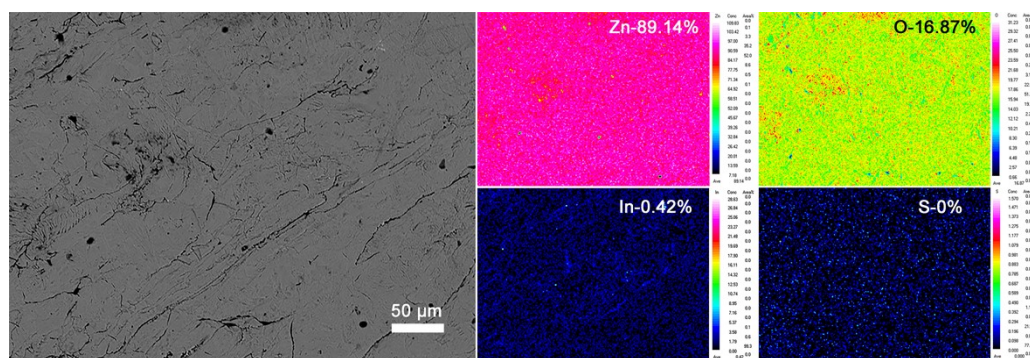


**Fig. S17** The EMPA/WDS element distribution of different elements for ZnIn alloy anode after 100 cycles.

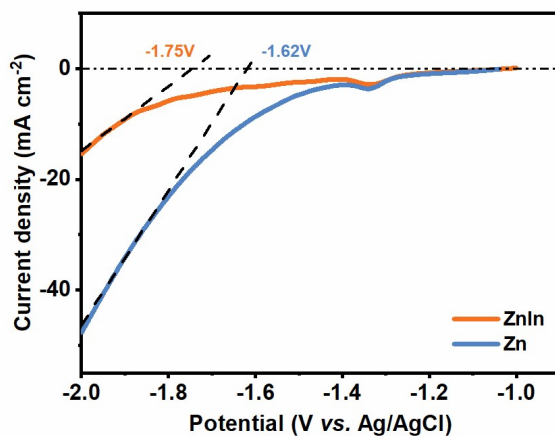


**Fig. S18** LSV curves of pure Zn and ZnIn alloy in 1 M Na<sub>2</sub>SO<sub>4</sub> at 5 mV s<sup>-1</sup>.

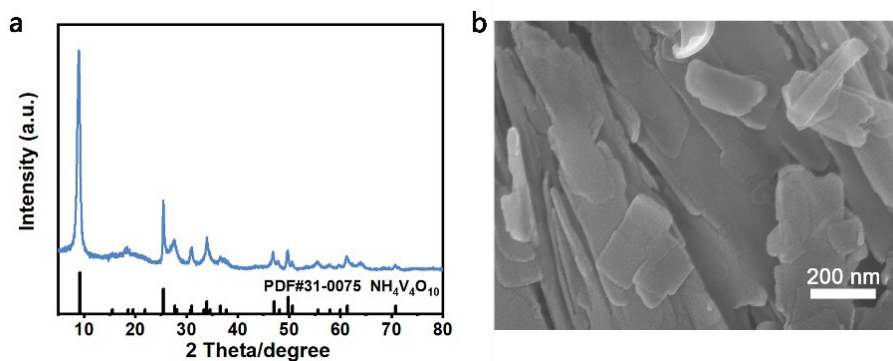


**Fig. S19** Characterization of NH<sub>4</sub>V<sub>4</sub>O<sub>10</sub> cathode. (a) XRD patterns. (b) SEM image.

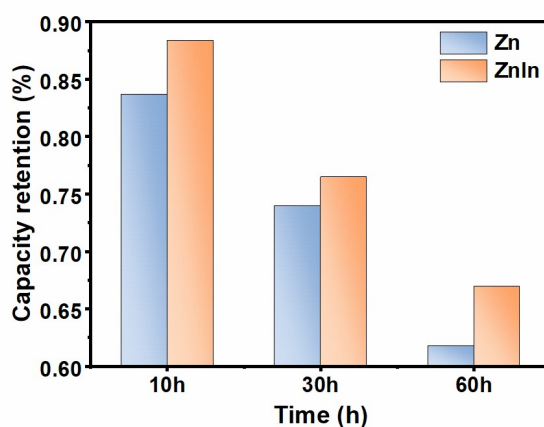


**Fig. S20** Self-discharge performance of ZnIn alloy and pure Zn after resting different times.

## References

1. Z. Guo, L. Fan, C. Zhao, A. Chen, N. Liu, Y. Zhang and N. Zhang, *Adv. Mater.*, 2021, **34**, 2105133.